JOURNAL OF GEOPHYSICAL RESEARCH, VOL. 99, NO. A2, PAGES 2471–2488, FEBRUARY 1, 1994

Landau damping of auroral hiss

D. D. Morgan, D. A. Gurnett, and J. D. Menietti
Department of Physics and Astronomy, University of Iowa, Iowa City

J. D. Winningham and J. L. Burch
Southwest Research Institute, San Antonio, Texas

Abstract. Auroral hiss is observed to propagate over distances comparable to an Earth radius from its source in the auroral oval. The role of Landau damping is investigated for upward propagating auroral hiss. By using a ray tracing code and a simplified model of the distribution function, the effect of Landau damping is calculated for auroral hiss propagation through the environment around the auroral oval. Landau damping is found to be the likely mechanism for explaining some of the one-sided auroral hiss funnels observed by Dynamics Explorer 1. It is also found that Landau damping puts a lower limit on the wavelength of auroral hiss. Poleward of the auroral oval, Landau damping is found in a typical case to limit $\omega/k_{\|}$ to values of 3.4×10^4 km/s or greater, corresponding to resonance energies of 3.2 keV or greater and wavelengths of 2 km or greater. For equatorward propagation, $\omega/k_{\|}$ is limited to values greater than 6.8×10^4 km/s, corresponding to resonance energies greater than 13 keV and wavelengths greater than 3 km. Independent estimates based on measured ratios of the magnetic to electric field intensity also show that $\omega/k_{\|}$ corresponds to resonance energies greater than 1 keV and wavelengths greater than 1 km. These results lead to the difficulty that upgoing electron beams sufficiently energetic to directly generate auroral hiss of the inferred wavelength are not usually observed. A partial transmission mechanism utilizing density discontinuities oblique to the magnetic field is proposed for converting auroral hiss to wavelengths long enough to avoid damping of the wave over long distances. Numerous reflections of the wave in an upwardly flared density cavity could convert waves to significantly increased wavelengths and resonance velocities.

1. Introduction

Auroral hiss is a commonly observed electromagnetic wave observed near the Earth's auroral regions. It has been known for many years that auroral hiss propagates in the whistler mode [see *Helliwell*, 1965]. The whistler mode propagates at frequencies below the electron cyclotron frequency or the electron plasma frequency, whichever is smaller [*Gurnett et al.*, 1983]. A number of early ground-based studies [*Burton and Boardman*, 1933; *Ellis*, 1959; *Morozumi*, 1962] established a connection between downward propagating auroral hiss and the visible aurora. Later, orbiting spacecraft made it possible to study auroral hiss within and near its source. By using data from Injun 3, *Gurnett* [1966] performed the first spacecraft study of auroral hiss. Gurnett's paper established the standard characteristics of auroral hiss, namely, the strong correlation with intense fluxes of field-aligned electrons of energies less than 10 keV, the location near the edge of the 40-keV electron trapping boundary, and the characteristic V shape of the spectrum. It was also pointed out that the emissions were approximately symmetric about the base of the funnel, but it was implied that in some cases the hiss was attenuated on one side. In a later paper, *Gurnett and Frank* [1972] again demonstrated the association of auroral hiss with electrons less than 10 keV in energy and correlated the occurrence of auroral hiss with electron inverted-V events. *Laaspere and Hoffman* [1976] further confirmed the association between electron beams of less than 1 keV and the occurrence of auroral hiss on the nightside of the Earth. Similar results were established by *Lin et al.* [1984] for dayside auroral hiss. These papers all showed that auroral hiss was generated in the auroral zone, and was related to low-energy electron beams.

The early studies of auroral hiss [e.g., *Gurnett*, 1966] were undertaken at low altitudes and dealt with downward propagating auroral hiss, as was demonstrated by *Mosier and Gurnett* [1969]. With the advent of DE 1 and other spacecraft it became possible to sample whistler mode emissions at higher altitudes. These studies showed that most of the auroral hiss observed at high altitudes ($>1R_E$) was propagating upward. Ray tracing done by *Gurnett et al.* [1983] for a single case indicated a source for auroral hiss around $1.8R_E$ geocentric distance, well below the spacecraft.

The auroral hiss events detected by DE 1 usually have a sharply defined upper cutoff frequency. On the dayside the upper frequency of auroral hiss corresponds closely with the local electron cyclotron frequency. On the nightside the upper frequency cutoff is believed to be at the local electron plasma frequency [*Persoon et al.*, 1983].

The funnel shape of the auroral hiss spectrum, which spreads out to follow the cutoff frequency, is easily observed and immediately identifies the event as upward propagating auroral hiss. A funnel-shaped spectrum from the Dynamics

Paper number 93JA02545.
0148-0227/94/93JA-02545$05.00

Explorer 1 (DE 1) spacecraft on September 18, 1981, is shown in Plate 1. The base of the funnel in this case is located at about 0752 UT or 69.8° invariant latitude (hereinafter INV). The funnel shape extends both poleward and equatorward of the base. *Gurnett et al.* [1986] established a clear connection between the base of the funnel and the source field line for whistler mode hiss generated by the electron gun aboard Spacelab 2. The base of the funnel is generally taken to indicate the L shell or invariant latitude of the source.

Smith [1969] first suggested that the funnel shape could be produced by propagation at wave normal angles near the resonance cone. This idea was explicitly demonstrated in several following papers, starting with *Mosier and Gurnett* [1969]. In this paper, ray tracing accurately reproduced the funnel shape. Other papers with similar comparisons include *James* [1976], *Gurnett et al.* [1983], *Lin et al.* [1984], and *Farrell et al.* [1988]. The Spacelab 2 active experiment also demonstrated that such V-shaped spectrums could be generated by an artificially produced electron beam [*Gurnett et al.*, 1986].

The generation mechanism of downgoing auroral hiss was initially thought to be incoherent Cerenkov radiation from a beam of precipitating electrons [see *Ellis*, 1957]. Eventually, *Taylor* [1973] showed that incoherent Cerenkov radiation falls some 2 orders of magnitude below the observed spectral density. *Maggs* [1976] attempted to explain the observed power in natural auroral hiss events with a convective beam instability. However, *Farrell et al.* [1989] pointed out that the mechanism proposed by Maggs fails for two reasons to explain the observed spectral density in the case of the Spacelab 2 hiss: first, the calculated wavelength is much larger than the source region, and, second, the wave spends too little time in the source region, severely limiting growth of the wave. In the case of hiss generated by an electron gun during the Spacelab 2 mission, *Farrell et al.* [1988] demonstrated that the power generated by the incoherent Cerenkov process falls 7 orders of magnitude short of generating the observed power. *Farrell et al.* [1989] then showed that sufficient power could be generated by a plasma bunching instability of the electron beam. The most likely generation mechanism for auroral hiss appears to involve an intermediate instability of the generating beam as put forward by *Farrell et al.* [1989].

Mosier and Gurnett [1969] used Injun 5 data to determine the Poynting flux direction of auroral hiss. The auroral hiss was shown to be propagating downward along the field line, in the same direction as the electron beam. *Farrell et al.* [1988] again demonstrated in the Spacelab 2 active experiment that $\mathbf{k} \cdot \mathbf{v}_{beam} > 0$. This result strongly implies that auroral hiss is generated entirely at the $m = 0$ or Landau resonance ($v_\parallel = \omega/k_\parallel$), since cyclotron resonance interactions would have propagation vectors directed opposite to the motion of the beam [*Farrell et al.*, 1988].

The purpose of this paper is to explore the effect of Landau damping on the propagation of auroral hiss. Landau damping is a collisionless process by which electromagnetic waves lose energy to charged particles with velocity near the resonance velocity $v_\parallel = \omega/k_\parallel$. It is important to study Landau damping because (1) its presence has a direct effect on the intensity of waves in the magnetosphere, and (2) its absence puts constraints on the properties of the wave, particularly the wavelength. In section 2 the observed intensity characteristics of auroral hiss will be discussed. Spectrograms of specific events will be presented. In section 3, the formula for the growth rate γ (i.e., the negative of the damping coefficient) will be simplified for the case of propagation near the resonance cone, assuming an isotropic electron distribution function. Some sample distribution functions will be discussed. In section 4, the ray tracing procedure will be discussed, and in section 5, sample rays will be traced and damping computed for each ray. Energy and frequency dependence of the damping will be tested. Finally, in section 6 the implications of the results from section 5 will be discussed.

The data utilized for the present research is from the Dynamics Explorer 1 (DE 1) spacecraft. Orbital parameters are documented by *Gurnett and Inan* [1988]. The advance in the line of apsides makes it possible to survey all geocentric distances between perigee and apogee at all latitudes over a period of years. Because of spacecraft rotation, fields and particles can be sampled as a function of direction as well as position. The instrument used to detect auroral hiss and other plasma wave phenomena is the plasma wave instrument (PWI), described by *Shawhan et al.* [1981]. The data of specific interest to us are from the step frequency correlator, which operates between 0.1 and 400 kHz. The frequency range of this instrument is divided into 128 logarithmically spaced steps with approximately 1% resolution.

The instrument on DE 1 that provided the plasma data used for this work is the high-altitude plasma instrument (HAPI), described by *Burch et al.* [1981]. The usual mode of operation is to sweep through 30 logarithmically spaced energies between 5 eV and 13 keV once per 0.5 s. The instrument consists of five electrostatic analyzers oriented at 45°, 78°, 90°, 102°, and 135° to the spacecraft spin axis. All detectors are used to detect ions, whereas only the 78°, 90°, and 102° detectors are used to detect electrons. Each detector has a full-width half-maximum acceptance angle of 10° in the azimuthal direction and 2.5° in the polar direction. Because the Earth's magnetic dipole is oriented about 12° from the Earth's rotation axis and because the loss cone in the sampled region is about 6°, the 78°, 90°, or 102° detector is always sampling the loss cone.

2. Attenuation Characteristics of Auroral Hiss

The top panel of Plate 1 shows the classical signature of auroral hiss on a frequency-time spectrogram. The intensity is indicated by a color bar, with red being most intense, and dark blue being least intense. This particular case is chosen as an example because the "funnel" shape of the spectrum is unobscured by other types of electromagnetic noise or multiple sources. The base of the funnel, presumed to coincide with the source field line, is at about 69.8° invariant latitude (INV). The funnel extends symmetrically north and south from this invariant latitude. The upper cutoff, clearly visible poleward of the source, is at the electron plasma frequency. The electron distribution for the same period is depicted in the bottom panel of Plate 1 on an energy-time spectrogram. The distribution function is indicated by a color bar, with red being most intense, dark blue being least intense, and black indicating intensities below the instrumental threshold.

Three regions are clearly distinguishable in the particle spectrogram. Between 65° and 70° INV the electron population varies on much shorter spatial scales than are evident in

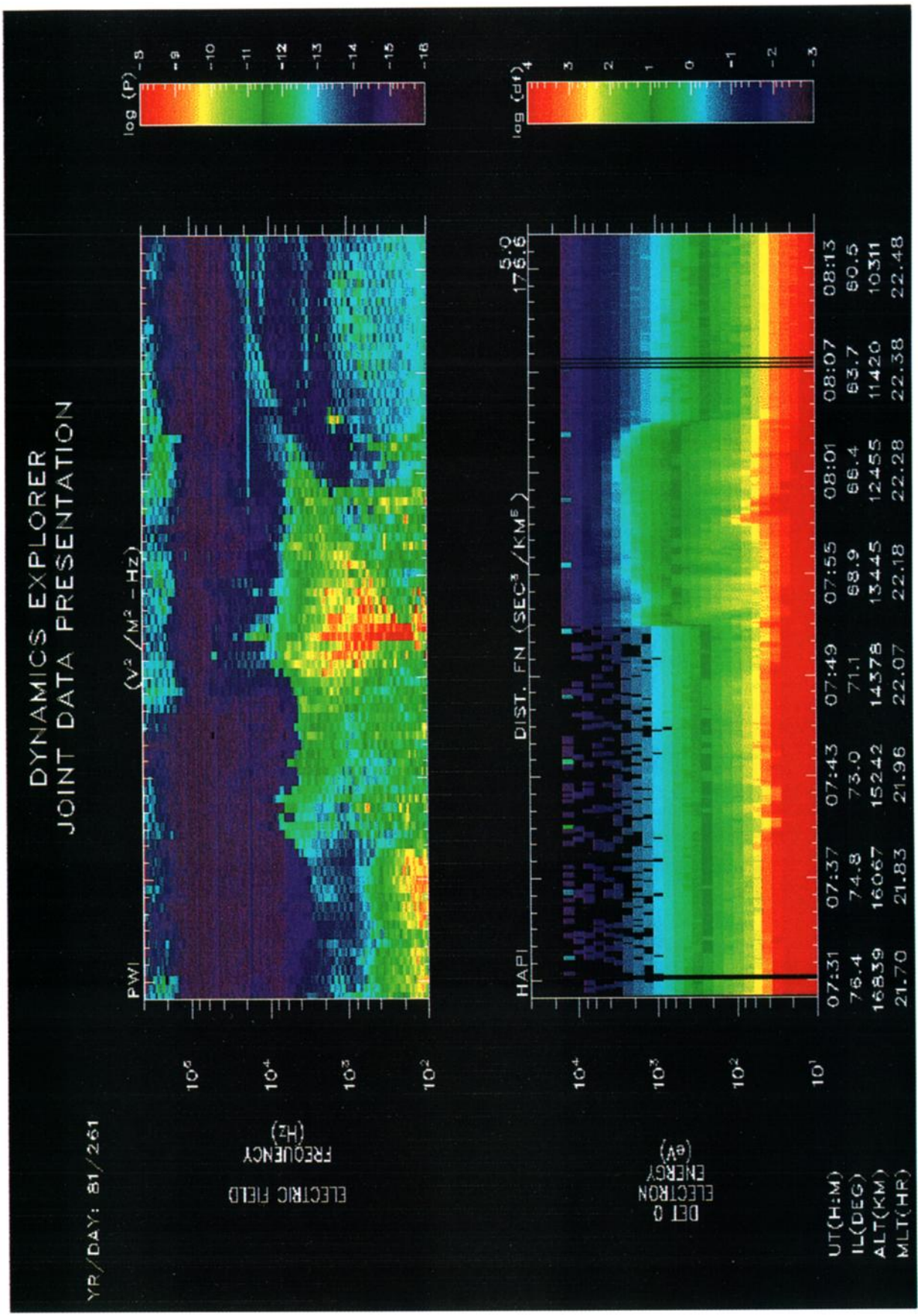

Plate 1. Spectrograms of an auroral hiss event on September 18, 1981. The top panel shows electric wave data from PWI; the bottom panel shows electron data from HAPI. The horizontal axis gives universal time and orbital parameters for both panels. The vertical axis give frequency for the upper panel and energy for the lower panel. Color gives wave intensity for the upper panel and electron distribution function for the lower.

other parts of the spectrogram. The disturbed region, which occurs around 70° INV, is associated with both diffuse and discrete aurora, containing both the central plasma sheet (CPS) and the boundary plasma sheet (BPS) [*Winningham et al.*, 1975]. We treat the BPS and CPS together as a single region and refer to it as the plasma sheet. Poleward of this region, electron energies are generally lower and the distribution function changes on a longer spatial scale than in the plasma sheet. We refer to this region as the polar cap. Equatorward of the plasma sheet, the electron distribution changes on longer spatial scales than in the plasma sheet, but energies are higher than in the polar cap. These electrons are associated by *Winningham et al.* [1975] with the lower-energy extension of the outer Van Allen radiation belt electrons. This region is nowadays referred to as the plasmasphere, and we shall refer to it thus.

The abrupt transition between polar cap and plasma sheet coincides with the auroral hiss source. The electron distribution function undergoes another abrupt transition at 67.5° INV as the spacecraft enters the plasmasphere. These electrons do not change on small spatial scales but are more energetic than the polar cap electrons. As the spacecraft passes out of the plasma sheet and into the plasmasphere, the auroral hiss goes through a minimum in intensity but then recovers and continues to propagate through the plasmasphere.

Plate 2 shows spectrograms similar to those in Plate 1 for an event on September 26, 1981. The base of the funnel in this case is obscured by broadband electrostatic noise [*Gurnett and Frank*, 1977] so that the source invariant latitude is not readily determined. The funnel shapes visible poleward and equatorward of the plasma sheet probably do not have the same base; that is, the auroral hiss has several sources. The auroral hiss propagates poleward unattenuated. The unattenuated poleward propagation coincides with a distribution function that falls off sharply at kilovolt energies over the polar cap. Although the funnel is visible equatorward (i.e., toward lower invariant latitudes), it fades out, first with a downward sloping intensity profile around 65° INV, then, after an increase, again around 64° INV. This fading out shows no indication of the plasma frequency cutoff feature seen poleward of the source in Plate 1. The strong equatorward attenuation coincides with a rise in energy of the electron distribution function.

Plate 3, for an event of October 5, 1981, shows many of the same features as Plate 2. Poleward, unattenuated propagation coincides with an electron distribution function that decreases below the instrument threshold at energies of about 1 keV. Equatorward, the hiss appears to be attenuated abruptly as it leaves the plasma sheet. This attenuation nearly coincides with an abrupt enhancement in the distribution function around 68.5° INV. Again, the plasmasphere electrons are more energetic than the polar cap electrons, although they are not as energetic as the plasma sheet electrons. Also, the plasmasphere electrons change on longer spatial scales than the plasma sheet electrons. It is probable that this auroral hiss event has multiple sources. There appears to be a continuous source between 71° and 69° INV. A discrete source is apparent around 68.6° INV and a weaker source probably exists near 68.0° INV. Finally, although the auroral hiss is observed to be attenuated abruptly at about 67.5° INV, it is not totally obliterated; there is still a trace of auroral hiss that continues to propagate equatorward. In this case, equatorward attenuation appears to take place in an almost discrete region that nearly coincides with a rise in electron energy.

Finally, we show a dayside case. Plate 4 shows an event at 1000 UT on September 26, 1981. The funnellike aspect of the auroral hiss is very clear. The smooth upper cutoff marks the electron cyclotron frequency rather than the electron plasma frequency. Generally, for dayside hiss f_c is less than f_p. There appears to be a strong source region between 70° and 71° INV. Also, there is a visible frequency minimum around 72.2° INV, which probably indicates another source. The faint line that falls irregularly between 1000 and 1020 UT at frequencies above the hiss funnel is upper hybrid resonance noise. When the upper hybrid emission is well above the cyclotron frequency, as in this case, it approximates the electron plasma frequency. Equatorward attenuation in this case coincides with changes in the upper hybrid frequency (f_{UHR}). A sharp attenuation takes place at about 68.2° INV almost coincident with an abrupt change in f_{UHR}. Another decrease in auroral hiss intensity occurs at 65.0° INV, coincident with another jump in f_{UHR}. There are no abrupt changes in the high energy electron distributions at these points. These coincidences indicate a role for density related reflections in attenuating auroral hiss. However, there is still a definite north-south asymmetry in the electron distribution. It is interesting to ask what the effect of the electrons on attenuation ought to be.

From these examples it is possible to make some generalizations. First, auroral hiss is observed to propagate for great distances in the Earth's magnetosphere. It can be estimated from spectrograms of the type shown in this section that auroral hiss can propagate at least $1.5R_E$ poleward from its source in the plasma sheet, in most cases with little or no attenuation. The second generalization is that auroral hiss is often less intense equatorward than poleward. This assertion is quantified later in this section. Third, electron distributions go to higher energies equatorward than poleward of the source.

Part of the motivation of this paper is to explore the connection between the last two of these assertions. Do the warm radiation belt electrons have an effect on the intensity of auroral hiss? From the discussion of the events in this section, it appears that electrons of over 1-keV energy can contribute to the attenuation of auroral hiss equatorward of the source. When this is not true, what constraints can be put on the auroral hiss?

A study of the available DE 1 wave data was conducted to quantify the assertion that auroral hiss is generally weaker equatorward than poleward of the source region. To conduct this study, 104 spectrograms of auroral hiss events were selected from the DE 1 PWI data set. This data set ranges from 1981 to 1987, although the amount of available data per year decreases sharply with advancing years. A spectrogram was eliminated from the data set if there was no possibility of seeing both sides of the funnel. A spectrogram was also eliminated if the spacecraft was not at a geocentric radial distance of greater than $2.0R_E$ during detection of one side of the funnel. This restriction is necessary because, when the spacecraft gets to low altitudes, it can go under the region where the auroral hiss is propagating, leading to shortening or even disappearance of the funnel.

The spectrograms were examined by eye to determine whether the intensity of auroral hiss was greater when it was

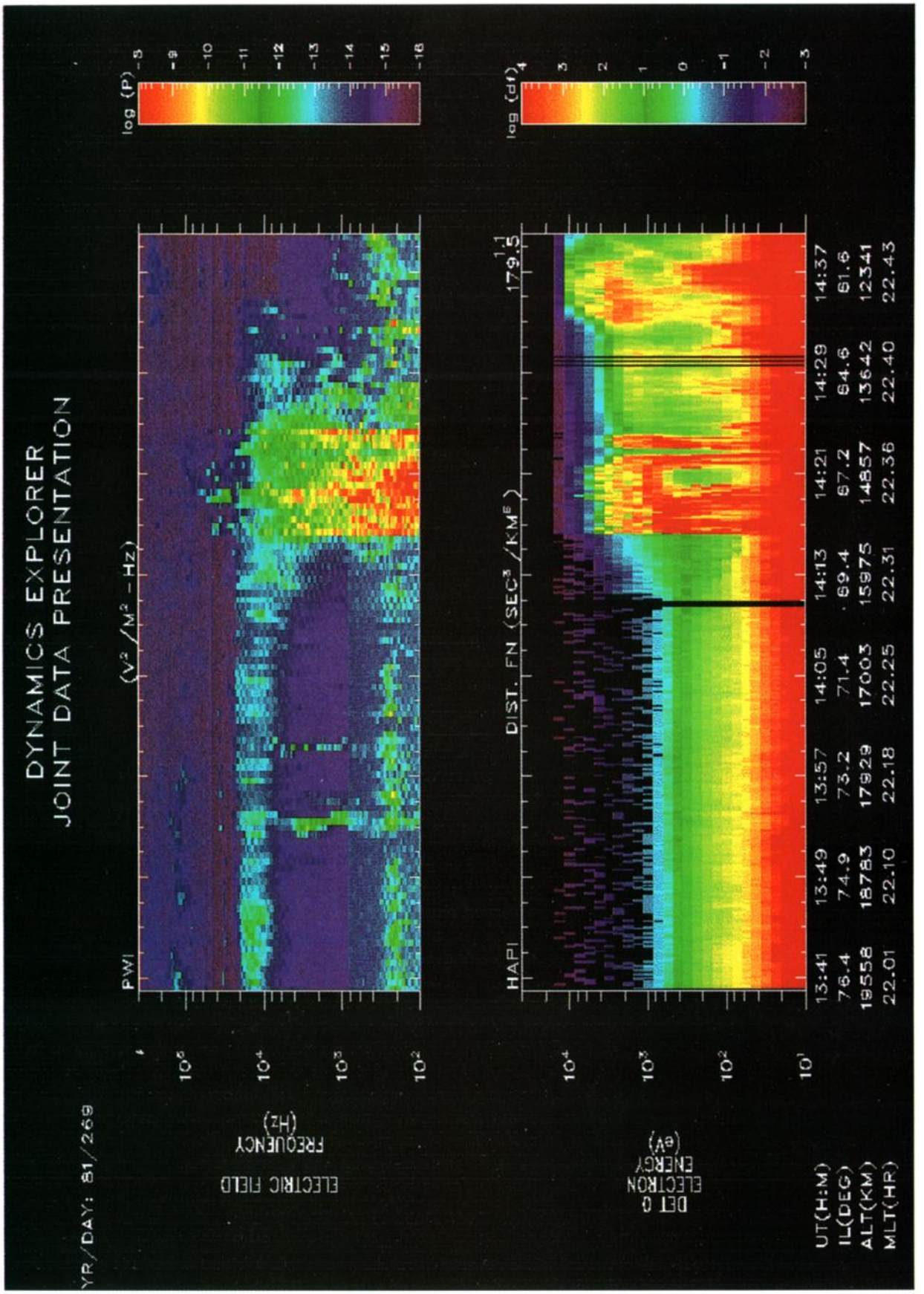

Plate 2. Spectrograms similar to those in Plate 1 of auroral hiss event on September 26, 1981.

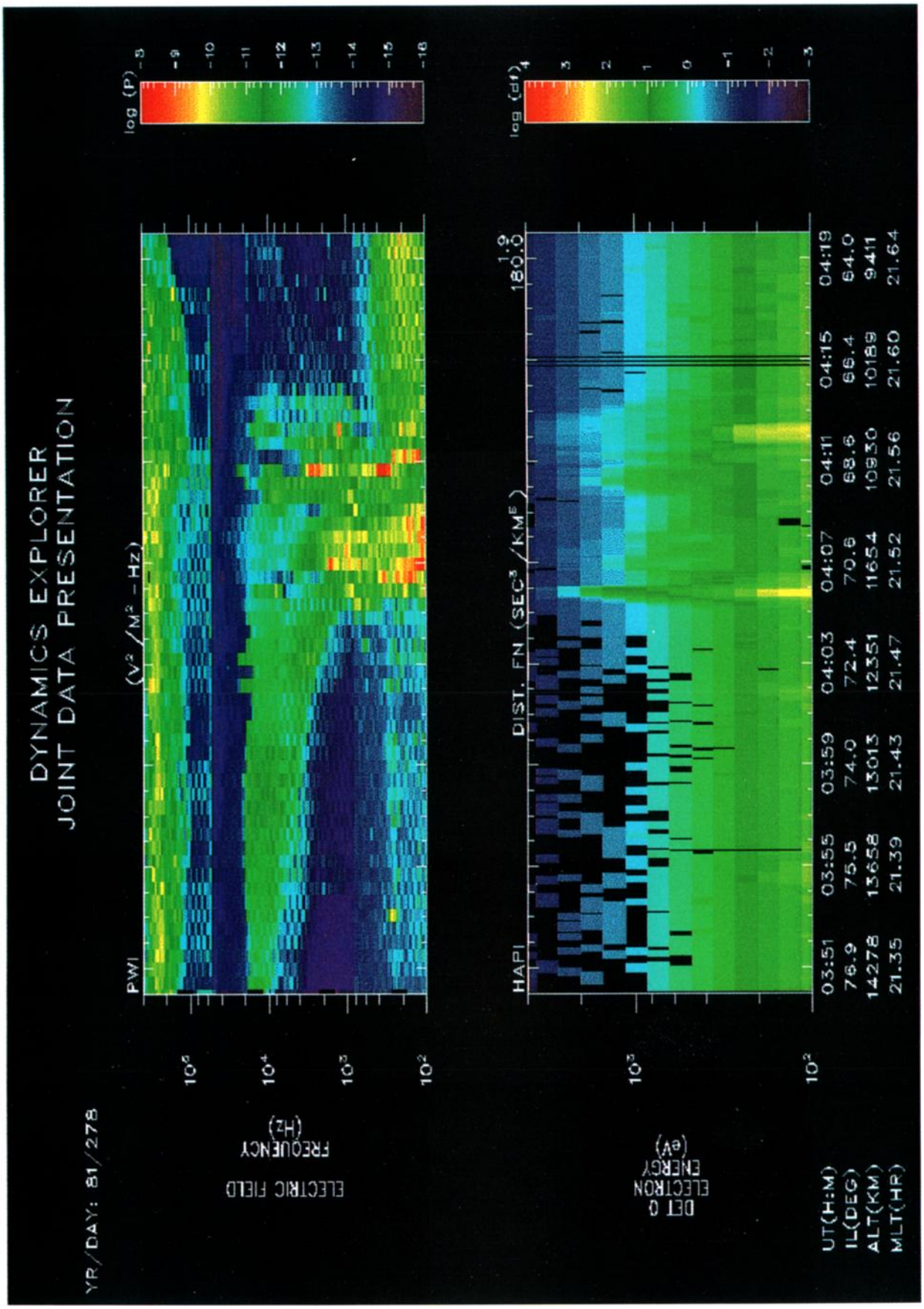

Plate 3. Spectrograms similar to those in Plate 1 of auroral hiss event of October 5, 1981.

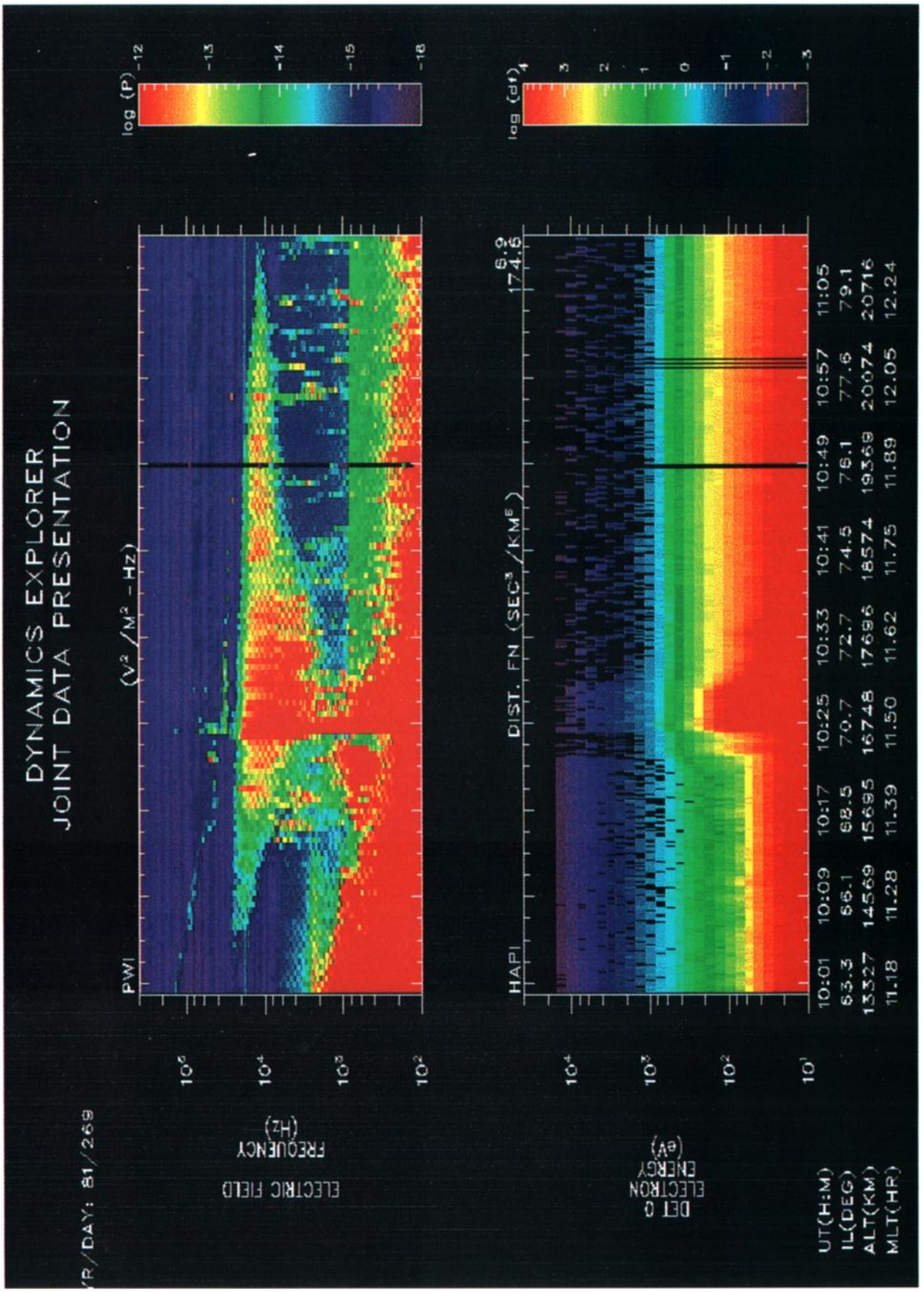

Plate 4. Spectrograms similar to those in Plate 1 of a dayside auroral hiss event at 1000 to 1100 UT, September 26, 1981.

Table 1. Relative Strength of Poleward and Equatorward Auroral Hiss

Comparison of Intensity	Number of Occurrences	Percentage of Occurrences, %
Equatorward > poleward	5	4.8
No difference	32	30.8
Poleward > equatorward	67	64.4

propagating poleward or equatorward. The results were tabulated in three categories: poleward intensity > equatorward intensity, poleward intensity < equatorward intensity, and poleward intensity ~ equatorward intensity. An event was tabulated in the third category if there was any doubt which side of the auroral hiss funnel was brighter. In the case of an "eyeball average" of this sort, a difference in intensity probably must be a factor of 10 to be clearly visible. The results are shown in Table 1. This study clearly establishes a tendency for auroral hiss to have higher intensities poleward than equatorward. Since electron populations tend to be more energetic equatorward than poleward of the plasma sheet, it is very plausible that Landau damping is responsible for at least part of this poleward-equatorward asymmetry.

3. Landau Damping

Collisionless damping is the mechanism by which a plasma wave loses energy to charged particles by accelerating or decelerating them. This interaction is strongest when particles come into resonance with the wave at the difference between the wave frequency and some harmonic of the particle cyclotron frequency. The resonance condition for species α is given by

$$v_{\parallel} = \frac{\omega - m\Omega_{c\alpha}}{k_{\parallel}} \tag{1}$$

This damping mechanism, when applied to Langmuir waves with $m = 0$, is known as Landau damping [*Landau*, 1946] and is discussed in many books on plasma physics [e.g., *Nicholson*, 1983]. If $m \neq 0$, this type of energy exchange is called cyclotron growth or damping. *Kennel* [1966, Equation (3.9)], gives the linear growth rate (i.e., the negative of the damping rate) for waves propagating in a collisionless, homogeneous, magnetized medium. His derivation assumes resonance energies well above the thermal velocity of the distribution function and small growth rates compared to the wave frequency. Kennel's formula is lengthy and is therefore not repeated here. Essential features of Kennel's formula are that it includes a sum over species, delta functions expressing the resonance conditions of each species as given by (1), an expression involving derivatives of the distribution functions of each species with respect to particle velocities perpendicular and parallel to the magnetic field direction, and integrals over velocities perpendicular and parallel to the magnetic field direction. Perpendicular and parallel subscripts in (1) and throughout this paper refer to components perpendicular and parallel to the magnetic field.

We list here a number of assumptions that simplify computation of the linear growth rate for whistler waves.

1. Auroral hiss propagates near the resonance cone. This assertion is strongly supported by references cited in previous sections. Because resonance cone propagation occurs as $n \to \infty$, its effect on the computation of the linear growth rate is that $n^2 \gg R$, L, and S, and $n^2 \sin^2\theta \gg P$, where R, L, P, and S are cold plasma parameters given by *Stix* [1962]. The resonance cone angle, θ_{Res}, is given by

$$\tan^2\theta_{\text{Res}} = -P/S \tag{2}$$

Since the resonance cone angle for auroral hiss is usually on the order of 1 rad, the $\sin^2\theta$ factor involved in the comparison to P is not so small as to be worrisome, and n^2 dominates all competing terms. Typically, R, L, P, and S are no greater than 5% of their competing terms in n^2.

2. Ions play a negligible part in the physics of collisionless damping. Since we are concerned with frequencies well above the lower hybrid resonance frequency, which is calculated to be about 500 Hz, ion effects need not be taken into account. In this paper, Ω_c and ω_p refer to electron cyclotron and plasma frequencies.

3. The auroral hiss we are dealing with occurs only on the nightside, and therefore $\Omega_c^2 \gg \omega_p^2 > \omega^2$. This assumption allows an important approximation in the computation of $\partial D^{(0)}/\partial\omega$, where $D^{(0)}$ is the cold plasma determinant.

4. Only the $m = 0$ term is significant. Cyclotron resonances occur only at relativistic energies where the electron population is not well known and is assumed to be very small.

5. The distribution function is isotropic. This assumption appears to be incorrect because electron distributions in and around the auroral region often incorporate a loss cone. However, we will show that the loss cone has little effect on the computation of the growth rate.

6. The quantity $|k_\perp v_\perp/\Omega_c| \ll 1$ where the distribution function is large. This quantity is the argument of Bessel functions J_m that appear in Kennel's formula. This assumption allows us to approximate J_0^2 by the value 1.

Use of assumptions 1 and 2 with Kennel's formula yields

$$\gamma\frac{\partial D^{(0)}}{\partial\omega} = \frac{8\pi^2 n^4\omega_p^2}{k^2|\cos\theta|}\int_0^\infty dv_\perp J_m^2\left[\frac{\partial F}{\partial v_\perp}\frac{m\Omega}{k} + \frac{\partial F}{\partial v_\parallel}\cos\theta v_\perp\right] \tag{3}$$

This is a general expression for a wave propagating close to the resonance cone where ion motion is not significant. In this expression, $F = F(v_\perp, v_\parallel)$ is the electron distribution function, and the integral is carried out over $v_\perp$ while $v_\parallel$ is a constant determined by (1). The function F is normalized to give 1 when integrated over all velocity space.

Assumption 3 taken in conjunction with assumptions 1 and 2 allows us to approximate the derivative of the zeroth-order index of refraction determinant. An exact expression comes from the definition of the cold plasma determinant given by *Stix* [1962]:

$$\frac{\partial D^{(0)}}{\partial\omega} = \left(\frac{\partial A}{\partial\omega} - \frac{4A}{\omega}\right)n^4 - \left(\frac{\partial B}{\partial\omega} - \frac{2B}{\omega}\right)n^2 + \frac{\partial C}{\partial\omega} \tag{4}$$

where A, B, and C are functions of the cold plasma parameters R, L, S, and P and the wave normal angle θ. Using assumption 1, which implies $n^2 \gg R$, L, P, and S, the first term will dominate all others because of the fourth power of n. Since the definition of the resonance cone requires that $A \to 0$, only one term remains to be considered:

Table 2. Comparisons: Three Ways of Computing γ, Two Ways of Computing $\partial D^{(0)}/\partial\omega$

E_{Res}, keV	γ, s^{-1} Numerical	γ, s^{-1} Numerical With Loss Cone	γ, s^{-1} Approximate	$\partial D^{(0)}/\partial\omega$ Numerical	$\partial D^{(0)}/\partial\omega$ Approximate
0.1	-3.262×10^3	-3.231×10^3	-3.290×10^3	3.315×10^3	3.154×10^3
.32	-8.698×10^2	-8.257×10^2	-8.809×10^2	3.225×10^2	3.075×10^2
1.0	-2.405×10^2	-2.287×10^2	-2.436×10^2	3.302×10^1	3.134×10^1
3.2	-6.488×10^1	-6.174×10^1	-6.573×10^1	3.186×10^0	3.020×10^0
10.0	-1.813×10^1	-1.725×10^1	-1.843×10^1	3.127×10^{-1}	2.963×10^{-1}

$$\frac{\partial D^{(0)}}{\partial\omega} \cong \frac{\partial A}{\partial\omega} n^4 \tag{5}$$

If we approximate θ by θ_{Res}, the expressions for P and S given by Stix can be used to give the derivative of A as

$$\frac{\partial A}{\partial\omega} = \frac{2(2\omega^2 - \Omega_c^2 - \omega_p^2)}{\omega(\omega^2 - \Omega_c^2)} \tag{6}$$

If $\Omega_c^2 \gg \omega_p^2 > \omega^2$, as usually occurs for nightside auroral hiss, then

$$\partial A/\partial\omega \simeq 2/\omega \tag{7}$$

is an adequate approximation, and

$$\partial D^{(0)}/\partial\omega \approx 2n^4/\omega \tag{8}$$

Table 2 shows results of computing $\partial D^{(0)}/\partial\omega$ numerically from the dispersion relation (given by *Stix* [1962, Equations (21)–(24)] and approximately from (8) for reasonable values of ω, ω_p, and Ω_c. The two values can be seen to correspond closely in each case. On the dayside, assumption 3 is usually not true, ω_p^2 being greater than Ω_c^2.

Assumption 4 allows us to eliminate the first term under the integral. Incorporating assumption 4 and (8) with (3) gives

$$\gamma = \frac{4\pi^2\omega_p^2\omega}{k^2|\cos\theta|} \int_0^\infty dv_\perp J_0^2 v_\perp \frac{\partial F}{\partial v_\parallel} \cos\theta \tag{9}$$

Assumption 5 allows us to set $v_\perp \partial F/\partial v_\parallel = v_\parallel \partial F/\partial v_\perp$. The value of $v_\parallel$ is fixed by (1), so that it may be factored out of the integral. Assumption 6 allows the remaining Bessel function, J_0 to be approximated by a value of 1. With these assumptions the integral can be performed, yielding the formula

$$\gamma = \frac{4\pi^2\omega_p^2}{k^2} \omega v_\parallel F(0, v_\parallel) \operatorname{sgn}(\cos\theta) \tag{10}$$

The Landau resonance condition, $v_\parallel = \omega/k_\parallel$, can be used to write (10) in the form

$$\gamma = \frac{-4\pi^2}{\omega} \omega_p^2 \operatorname{sgn}(\cos\theta) v_\parallel^3 \cos^2\theta F(v_\parallel) \tag{11}$$

where $F(v_\parallel) = F(0, v_\parallel)$. The distribution function F from Kennel's formula is normalized by the electron density, whereas the distribution function data received from the HAPI instrument is an absolute distribution function in units of particles s^3/km^6. The distribution function as detected by the HAPI instrument is here denoted by $\mathcal{F} = n_e F$. In SI units, $\omega_p^2 = n_e^2/\varepsilon_0 m_e = 3.183 \times 10^3$ n(/m^3) (cycles/s)^2. A division by 10^{18} is necessary to convert from kilometers to meters in the distribution function. Multiplying all numerical constants gives the formula for the Landau growth rate

$$\gamma = \frac{-1.257 \times 10^{-13}}{\omega} \operatorname{sgn}(\cos\theta) \cos^2\theta v_\parallel^3 \mathcal{F}(v_\parallel) \tag{12}$$

Note that the growth rate is negative, indicating damping. Growth is not possible according to this formula because an isotropic distribution function is assumed.

To establish the validity of the approximations involved in deriving (12), we will compare it with results computed numerically directly from (9). Since (9) and (12) involve the distribution function, we digress here to discuss how the distribution functions are evaluated.

Electron spectrograms shown in Plates 1–4 exhibit similar patterns of electron flux from the polar cap to the plasmasphere. Over the polar cap, electron energies are low, with the distribution function approaching zero between 1 and 10 keV. In the plasma sheet the electrons are more energetic and change on comparatively short spatial scales. In the plasmasphere the electron distribution function changes on larger spatial scales than in the plasma sheet but is more energetic than in the polar cap. Because the objective of this work is to extract a general result rather than model a particular event, we take a representative event and compute average distribution functions over extended times. Before proceeding, however, it is useful first to look at contour plots of distribution functions in the three regions. The sample event is that of October 5, 1981, chosen because it clearly exhibits both attenuation and propagation equatorward of the source region.

Figures 1, 2, and 3 show contour plots of the electron distribution functions at 0400, 0412, and 0417 UT, respectively. These three plots represent the distribution function in the polar cap, at an energy maximum in the plasma sheet, and in the plasmasphere, respectively. Over the polar cap, unattenuated propagation of auroral hiss is virtually always observed. The distribution shown in Figure 1, measured in the polar cap, is less energetic and more isotropic than those of the plasma sheet and the radiation belt. No loss cone is visible. Figure 2 shows the distribution function at a point toward the equatorward side of the plasma sheet. The electron distribution is at an energy maximum according to Plate 3. The auroral hiss undergoes attenuation nearly coinciding with the spacecraft passing through this maximum. The values of the distribution function are visibly higher

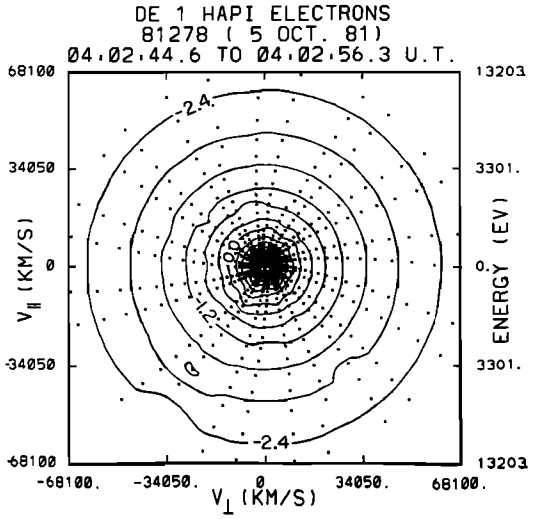

Figure 1. Contour plot of distribution function over the polar cap for event of October 5, 1981. Horizontal and vertical axes show $v_\perp$ and $v_\parallel$, respectively, in units of kilometers per second. The numbers labeling the contours are the base 10 logarithm of the value of the distribution function in units of particles s^3/km^6.

throughout this plot than those for the polar cap. Another difference between the two distributions is that the loss cone is clearly visible at low energies in the plasma sheet. Apart from the loss cone, this distribution function is isotropic. Figure 3 shows the distribution function in the plasmasphere. This distribution is less energetic than that in the plasma sheet, except that values of the distribution function at high energies are maintained. The loss cone is not distinguishable.

The contour plots just shown do not reflect the variation of the actual measurements made by the HAPI instrument because they are deliberately smoothed. Examination of the angle dependence of the measurements reveals a high level of angular fluctuation in the data. In particular, at high energies ($\gtrsim$1 keV) in the polar cap the count rate becomes

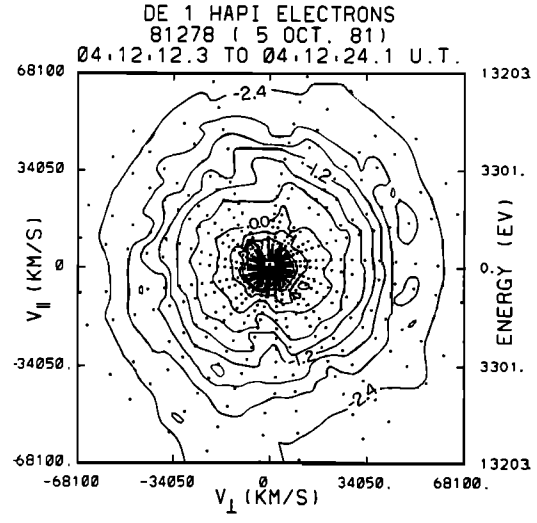

Figure 2. Contour plot of distribution function in the plasma sheet for event of October 5, 1981. Axes and units are as in Figure 1.

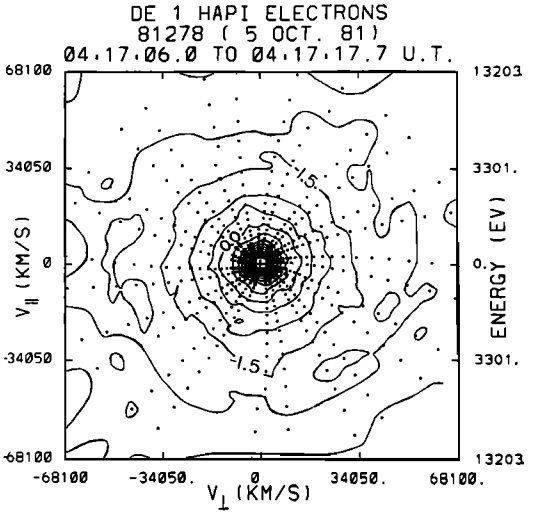

Figure 3. Contour plot of electron distribution function in the plasmasphere for event on October 5, 1981. Axes and units are as in Figure 1.

quite low, and the variation of the measured distribution function is of the same size as the measurements. At these energies the loss cone is difficult if not impossible to pick out and the variation of the distribution function appears to be random. Except for the loss cone, it is unlikely that the large fluctuations are due to real variation in the distribution function. It will be shown that the effect of a loss cone on the growth rate is minimal. Thus it makes sense to average the distribution function over pitch angle.

Ten sample distribution functions were taken in the polar cap and in the plasma sheet. Each sample consisted of data taken by HAPI during four spacecraft spins. All samples were averaged over pitch angle and then averaged with each other. The results are shown in Figures 4 and 5 in log-log form. The plasma sheet distribution is quite similar to the plasmasphere distribution and is not shown here.

The fact that these plots have regimes in which the distribution function versus energy gives roughly a straight line indicates that this portion of the distribution function

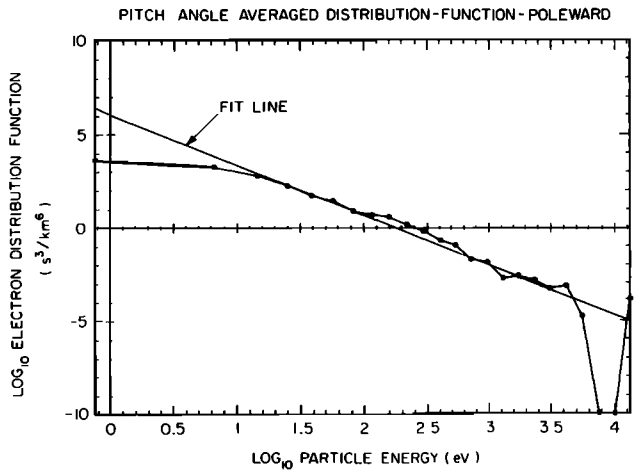

Figure 4. Log-log plot of an angle and time averaged distribution function. Several samples of the distribution function over the polar cap have been averaged.

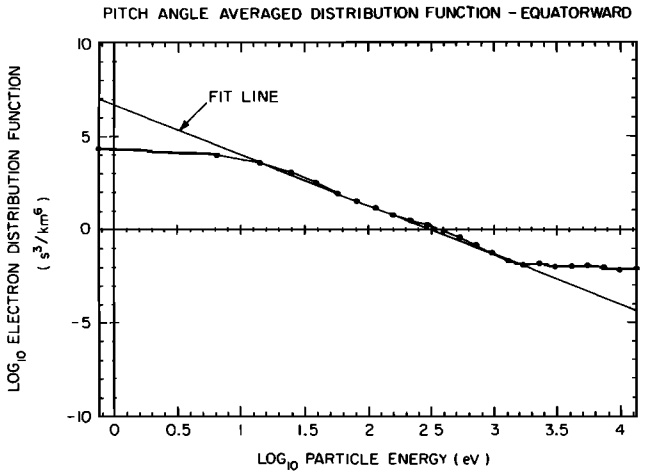

Figure 5. Angle and time-averaged distribution function from the plasmasphere for event of October 5, 1981.

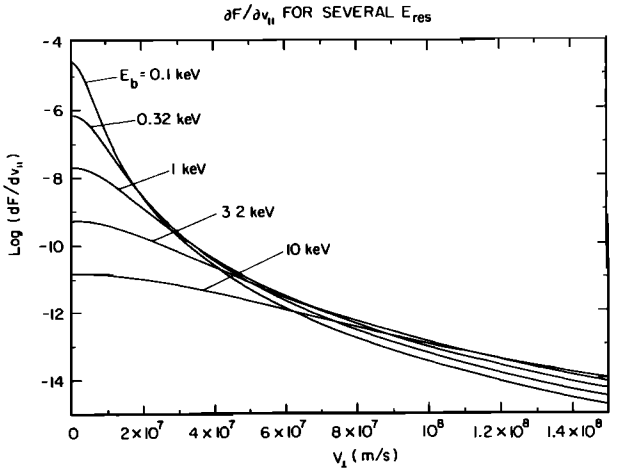

Figure 6. The base 10^n logarithm of $\partial\mathcal{F}/\partial v_\parallel$ for a sample calculation of γ. The fit line in Figure 4, given by (13b), is the model of the distribution function used.

can be thought of as a power law. This is an oversimplification. A cursory glance at Figures 4 and 5 reveals several different regimes. Over the polar cap the distribution function goes to zero at around 5 keV and recovers to nonzero values around 13 keV. It is normal for distributions over the polar cap to go abruptly to zero. The plasma sheet distribution displays a distinct high energy tail above 1.5 keV. This type of distribution is not unusual. In order to have idealized functions to deal with, a fit has been taken of the points seen to lie on a straight line. This operation yields the result that the distribution functions are given by

$$\mathcal{F}(E) = \frac{1.057 \times 10^6}{[E(\text{eV})]^{2.619}} \left[\frac{\text{s}^3}{\text{km}^6}\right] \tag{13a}$$

for the polar cap distribution function, and

$$\mathcal{F}(E) = \frac{5.408 \times 10^6}{[E(\text{ev})]^{2.632}} \left[\frac{\text{s}^3}{\text{km}^6}\right] \tag{13b}$$

for the plasmasphere distribution function. Equation (13b) is now used as the distribution function in testing (12) for computing γ. Use is made of ray tracing results that are explained in the next section. We will compare the results of (12) with the results of numerically integrating Equation (9) for the power law (13b) and for (13b) modified to include a 10° loss cone.

In using (9), 100 points are taken between $v_\perp = 0$ and $v_\perp = 1.5 \times 10^8$ m/s, where the integrand is small compared to its maximum value in all cases. Simpson's rule [see *Apostol*, 1969] is used to integrate over each triplet of points. Figure 6 shows values of the derivative for a sample position along a ray path taken at different beam energies. As the resonance velocity gets larger, the importance of the high energy tail is relatively increased. However, calculation of J_0^2 shows that as the resonance velocity gets larger, the range of values for which J_0^2 is close to 1 is also expanded. Thus this approximation is good for all energies shown.

Figure 7 shows $\partial\mathcal{F}/\partial v_\parallel$ for the same set of parameters but with (13b) modified to simulate a 10° loss cone. The only visible effect is at very small values of $v_\perp$. Because of the factor $v_\perp$ in the integrand of expression (9), the effect on the integral is very small.

Results of the three calculations of γ are shown in Table 2. The three methods yield very similar results. Thus (12) ought to be a good method of calculating γ at high resonance energies. Equation (12) will be used in section 5 to compute γ using interpolated values of $\mathcal{F}(v_\parallel)$ from a table of distribution function versus energy.

Spacecraft charging was estimated for purposes of correcting the estimated distribution functions. However, because resonance energies are chosen in the range between 0.1 and 10 keV and the spacecraft potential is always below 20 eV, spacecraft charging does not significantly affect the conclusions of this work. Therefore the effect of spacecraft charging will not be discussed further.

Once the growth rate has been computed, it is necessary to integrate the growth rate along the path to give the total growth. This is accomplished by computing the integral

$$\Gamma = \int_{\text{path}} \frac{\gamma}{V_g}\, ds \tag{14}$$

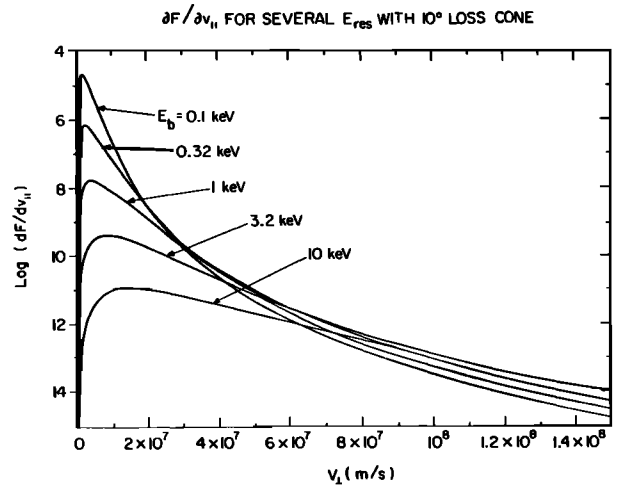

Figure 7. Same as Figure 6 except that the model distribution function now has a loss cone of 10°. The effect of the loss cone is evident only very close to $v_\perp = 0$.

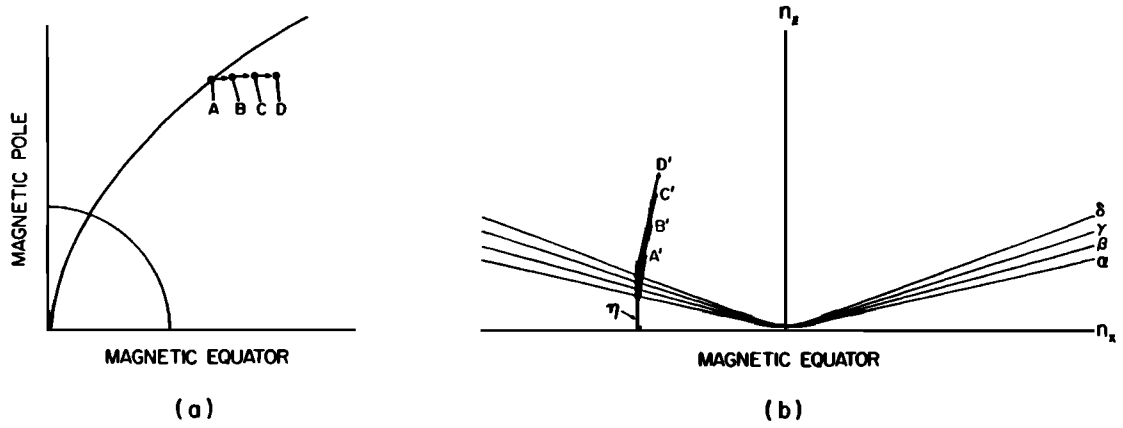

Figure 8. Schematic diagram illustrating the ray tracing procedure. (a) Progress of the ray in space. (b) Progress of the index of refraction components.

where Γ is the integrated growth rate, γ the growth rate at a given point, V_g the group velocity at a given point on the ray path, and the integral is taken along the calculated ray path. A trapezoidal formula [see *Apostol*, 1969] is used to perform the integration. The integrated growth rate Γ can be interpreted as follows. If the magnitude of the wave electric field at the beginning of the ray is E_0, then the magnitude at point A along the path is

$$E_A = E_0 e^{\Gamma} \tag{15}$$

This means that the change in intensity along the ray path is given by

$$P(A)/P(r_0) = e^{2\Gamma} \tag{16}$$

Thus small changes in Γ cause large changes in intensity.

4. Ray Paths

The calculation of Landau damping of auroral hiss requires knowledge of the ray path. The most general method of ray tracing uses the Haselgrove equations, the wave analogs of Hamilton's equations. The Haselgrove method was not chosen for this work because it has computational problems for rays propagating near the resonance cone. Since resonance cone propagation is precisely the regime in which we are interested and since the present work does not require an extremely high degree of accuracy, we have chosen a very simple ray tracing scheme known as the Poeverlein construction. An account of it is given in many books on plasma waves [e.g., *Budden*, 1985]. The Poeverlein construction uses two simple principles: Snell's law, and the fact that the ray path is normal to the index of refraction surface. For simplicity, the medium is assumed to change only in the magnetic field direction. Only propagation in the magnetic meridian plane is considered.

Under the given geometric conditions, Snell's law reduces to a statement that the component $n_\perp$, perpendicular to the magnetic field, remains constant as the ray propagates. The cold plasma dispersion relation is given by *Stix* [1962]. By utilizing the definitions $n_\perp = n \sin\theta$ and $n_\parallel = n \cos\theta$ the dispersion relation is easily put into a quadratic form that can be solved for $n_\parallel$:

$$Pn_\parallel^4 + [(P+S)n_\perp^2 - 2PS]n_\parallel^2 + [Sn_\perp^4 - RLn_\perp^2 + PRL] = 0 \tag{17}$$

If the position in space is known, then R, L, P, and S are calculable as functions of ω, ω_p, and Ω_c. The value of $n_\perp$ is determined from the launch condition chosen for the ray. Thus at any given position the index of refraction and wave normal angle can be calculated.

To advance the ray path, (17) is differentiated to give the normal to the index of refraction surface. If ψ is the ray path angle with respect to the magnetic field, differentiation of (17) results in

$$\tan\psi = \frac{dn_\parallel}{dn_\perp} = \frac{-(S+P)n_\perp n_\parallel^2 - 2Sn_\perp^3 + RL\, n_\perp}{2Pn_\parallel^3 + [(S+P)n_\perp^2 - 2PS]n_\parallel} \tag{18}$$

To launch the ray, we assume that the auroral hiss is generated by an electron beam at energy E_{res} in the Landau resonance. The condition for the Landau resonance is

$$v_{res} = \frac{\omega}{k_\parallel} \tag{19}$$

where $v_{res} = (2E_{res}/m_e)^{1/2}$. Since $k_\parallel = (n\omega/c)\cos\theta$, this equation reduces to

$$\frac{v_{res}}{c} = \frac{1}{(n\cos\theta)} = \frac{1}{n_\parallel} \tag{20}$$

With the value of $n_\parallel$ determined by the beam energy the initial value of $n_\perp$ can be found from (17).

The ray tracing procedure is summed up in Figure 8. A source position and a generating beam energy are chosen. The component $n_\parallel$ is computed from (20). At the starting position, position A in Figure 8a, ω_p and Ω_c are calculated, leading to values for the cold plasma parameters. The cold plasma parameters with (20) determine the index of refraction curve at point A, labeled α in Figure 8b. Equation (17) is then solved for $n_\perp$. Thus $n_\perp$ and $n_\parallel$ are known for the starting position. The index of refraction at the launch point of the ray is labeled A′ in Figure 8b. The ray direction is the perpendicular to the index of refraction direction and is given by the arrow emerging from point A′. This direction is

calculated from (18). The ray is stepped in the direction indicated by the arrow. At this new position, ω_p and Ω_c are calculated anew, giving new values of the cold plasma parameters. Thus, using (17), curve β can be computed. The line η is a line of constant $n_\perp$ and goes through point A'. The next index of refraction point, B', is the point where curves η and β intersect. Point B' gives the new value of $n_\parallel$, the value of $n_\perp$ remaining the same. The value of $n_\parallel$ can be found by solving (17) for $n_\parallel$. The arrow at point B' gives the direction from point B to point C in Figure 8a. This direction is again given by (18). At point C, ω_p and Ω_c can be recalculated, leading to new values of the cold plasma parameters. From these values the curve γ can be computed. The intersection of η with γ gives the new $n_\parallel$, and the arrow at this point, C', gives the direction for getting to point D in Figure 8a, and so on.

Another quantity that is necessary for computation of the integrated growth rate given in (14) is the group velocity $\mathbf{V}_g$. The definition of group velocity is given by

$$\mathbf{V}_g = \frac{\partial \omega}{\partial \mathbf{k}} \tag{21}$$

This quantity is straightforward to compute from the cold plasma dispersion relation. Thus $\mathbf{V}_g$ can be computed exactly within the limits of the model.

A word should be said about the magnetic field and plasma density models that were used in this calculation. The magnetic field is computed from a standard Earth-centered dipole model of strength 3.1×10^{-5} T at the magnetic equator at the Earth's surface. The electron density is estimated from the auroral hiss upper frequency cutoff and is assumed constant. Since the path lengths that we calculate are less than an Earth radius, variations in the plasma density are believed to be relatively unimportant. Since there is no way to measure the spatial variation of the plasma density away from the spacecraft, a single representative density over the duration of a given event has been assumed.

The ray tracing scheme has three important limitations. First, we are unable to evaluate east-west propagation. Second, the plasma frequency is assumed to be constant. Third, no variation of the cyclotron frequencies is allowed perpendicular to the magnetic field direction. In particular, the assumption that the gradient of the magnitude of the magnetic field is along the magnetic field direction introduces a small error into the calculations. The angle between $\mathbf{B}$ and ∇B is usually about 20°. The error in the ray path calculations due to this effect is probably small compared to the error due to the assumption of constant plasma frequency, particularly in the perpendicular direction. Therefore we ignore this discrepancy.

5. Comparison With Observations

The techniques discussed in the previous sections are used to discuss a test case of auroral hiss propagation and damping. The distribution functions used are the average distribution functions displayed in Figures 4 and 5. We assume a likely auroral hiss source location at $R = 2.5R_E$ and $\lambda_{INV} = 70°$. Ray tracing is performed assuming a constant plasma frequency of 20 kHz and the usual magnetic field with a dipole moment of 3.1×10^{-5} T R_E^3. Starting at the source point, each ray is traced until it reaches a point 2.5° INV away from the source invariant latitude.

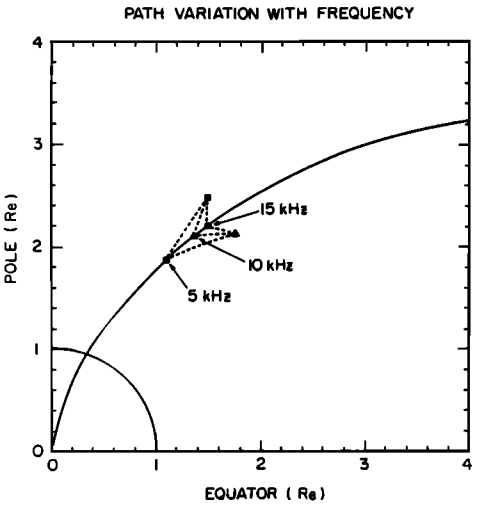

Figure 9. Ray path variation with frequency. Because lower-frequency waves propagate at a smaller angle from the magnetic field direction, they have longer path lengths.

It is important to point out again the limitations of this approach and how these limitations apply in the present case. As mentioned earlier, the ray tracing approach adopted here does not include the possibility of density variation in the direction perpendicular to the magnetic field. This precludes taking into account phenomena like density cavities [see *Persoon et al.*, 1986] or the plasmapause, two important phenomena that might have an effect on the propagation of the auroral hiss waves. The source region for the auroral hiss is in fact in the same region as the observed density cavities, and it may be that the auroral hiss that we observe is generated in a region of reduced density. The rays traced here should be taken as a modeling of the auroral hiss propagation outside of the plasma sheet and away from the observed density cavities. What is cited as a resonance energy is the energy corresponding to the resonance velocity $\omega/k_\parallel$ at the point that we start tracing the ray. This resonance velocity evolves somewhat during the transit of the wave. Since the frequency of the wave is known, the resonance velocity determines the magnitude of the propagation vector and therefore the wavelength of the auroral hiss. The main result of this section is to place a limit on the wavelength of auroral hiss.

As stated in the previous section, auroral hiss propagates in three regions of the magnetosphere labeled the polar cap, the plasma sheet, and the plasmasphere. We do not attempt to compute damping in the plasma sheet, since it involves modeling a distribution function that varies significantly on short spatial scales. We are more interested in exploring what happens to an auroral hiss wave once it leaves the source region either poleward or equatorward. However, as is evident from Plate 3 near 68.2° INV, it is likely that in some cases heavy damping occurs in very localized areas of high electron energy. This situation is not taken into account.

Figure 9 shows the effect on the ray path of varying the frequency. This figure shows that lower-frequency waves have longer ray paths. Variations in $\omega/k_\parallel$ have almost no effect on the ray path as long as the propagation vector is near the resonance cone.

Table 3. Variation of Damping With Beam Energy Summary of Results

	γ, s^{-1}		2.5° INV From Source		$P(1)/P(0)$	
E_{Res}, keV	Poleward	Equatorward	Poleward	Equatorward	Poleward	Equatorward
0.1	-7.2×10^2	-3.2×10^3	-3.6×10^3	-1.5×10^3	...	...
0.32	-4.0×10^2	-1.3×10^3	-1.1×10^2	-3.5×10^2	...	...
1.0	-4.6×10^1	-2.3×10^2	-7.2×10^0	-3.5×10^1	5×10^{-7}	4.0×10^{-31}
3.2	-1.1×10^1	-2.4×10^2	-9.8×10^{-1}	-2.1×10^1	1.4×10^{-1}	5.8×10^{-19}
10.0	~0	-9.5×10^2	-4.1×10^{-3}	-4.6×10^{-1}	9.9×10^{-1}	1.1×10^{-40}

Table 3 shows the results of computing the damping along the ray path for 10 kHz shown in Figure 10 for values of $\omega/k_{\|}$ corresponding to resonance energies of 0.1, 0.32, 1.0, 3.2, and 10.0 keV. Values of γ shown should be interpreted as representative, since this number varies along the ray path. Values of Γ are tabulated 2.5° INV from the launch point of the ray. Poleward damping is computed using the distribution function shown in Figure 4. Equatorward damping is computed using the distribution function shown in Figure 5.

Results poleward of the source region show that we do not expect auroral hiss generated at $\omega/k_{\|}$ less than 3.4×10^4 km/s (i.e., resonance energies less than 3.2 keV) to survive without substantial damping. At a resonance energy of 3.2 keV the calculated auroral hiss intensity falls off by nearly an order of magnitude within 2.5° INV, while at 10 keV, there is almost no damping. Observations indicate that auroral hiss undergoes little or no damping poleward of the source region within 2.5° INV. Thus, if these resonance energies are characteristic of beam energies at which auroral hiss is generated, the beams must have energies greater than 3.2 keV. This effectively puts an upper limit on $k_{\|}$ of 1.9×10^{-3} m^{-1}. For a wave normal angle of $\theta \approx 1$ rad, the wavelength must be greater than about 2 km.

Table 3 also shows damping in the equatorward direction. Two differences between the poleward and equatorward cases are apparent. First, the values of the damping coefficient in the equatorward direction are much larger than in the poleward case. Second, the highest energy does not give the lowest damping, as with the poleward case. A glance at Figure 5 indicates why this is the case. The distribution function has a high-energy tail that maintains the value of $\mathcal{F}$ at a roughly constant value while $v_{\|}$ becomes larger. Thus the value of the damping coefficient (that is $-\gamma$) grows as the resonance energy gets larger.

The lowest damping equatorward is for $\omega/k_{\|} = 1.9 \times 10^4$ km/s corresponding to a 1-keV resonance energy. According to this calculation, the intensity must fall off by twenty orders of magnitude over 2.5° INV. In other words, the auroral hiss should be damped to negligible amplitudes almost immediately after it is generated. Since the high-energy tail that causes this damping extends beyond the upper energy limit of HAPI, we take the HAPI limit, 13 keV as a lower limit on transmitted wave resonance energy. The corresponding value of $\omega/k_{\|}$ is 6.8×10^4 km/s. Values of $k_{\|}$ for this resonance velocity are about 1.0×10^{-3}/m. For a wave normal angle $\theta \approx 1$ rad, the wavelength λ is found to be greater than 3 km.

We have confirmed that auroral hiss has a minimum wavelength of the order of a kilometer by measuring ratios of magnetic to electric field, B/E, for three of the passes presented in section 2. For the events of September 18, 1981, shown in Plate 1, September 26, 1981, 1000 UT, shown in Plate 4, and September 26, 1981, 1300 UT, shown in Plate 2, we have measured values of $|E|^2$ and $|B|^2$ from line spectra at selected times. The ratio $|B|^2/|E|^2$ can be calculated from the linear Fourier analyzed Maxwell equations and is given by

$$\frac{|B|^2(\mathrm{nT})^2}{|E|^2(\mathrm{V/m})^2} = \frac{10^{18}}{9 \times 10^{16}(\mathrm{m/s})^2} \frac{n^2 + n_{\|}^2\left(\frac{S - n^2}{D}\right)^2 \left(\frac{P}{P - n_{\perp}^2}\right)^2}{1 + \left(\frac{S - n^2}{D}\right)^2 \left[1 + \left(\frac{n_{\|} n_{\perp}}{P - n_{\perp}^2}\right)^2\right]} \quad (22)$$

Equation (22) does not take into account the antenna orientation with respect to the field direction. Since auroral hiss probably comes from a sheetlike source or a number of linelike sources arranged in a sheetlike region, and from a range of altitudes, this is as precise as we can be without an extensive analysis. In using this formula the plasma parameters P, S, and D are calculated from a dipole magnetic field and a value of the plasma frequency obtained from various spectral features. For a measured $|B|^2/|E|^2$ ratio, (22) and

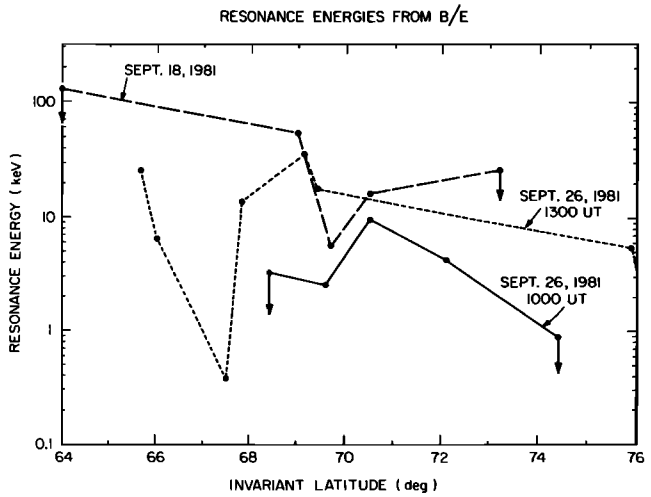

Figure 10. Independent computations of the resonance energy of auroral hiss based on the magnetic to electric field ratio for selected times of three events. These computations confirm the general result that resonance energies of auroral hiss waves are around or greater than a kilovolt. These resonance energies generally correspond to wavelengths of about a kilometer or more.

Table 4. Variation of Damping With Frequency

Frequency, kHz	γ, s^{-1}	V_g, m/s	Path Length, m	Γ	$P(1)/P(0)$
5	6.5×10^0	2.2×10^7	4.6×10^6	−1.4	6.1×10^{-2}
10	1.3×10^1	2.0×10^7	2.5×10^6	−1.7	3.3×10^{-2}
15	2.0×10^1	1.5×10^7	1.8×10^6	−2.4	8.2×10^{-3}

the dispersion relation (17) can be solved simultaneously to give both components of the index of refraction, $n_\perp$ and $n_\parallel$. The resonance energy v_{res} can then be calculated from $n_\parallel$ using (20). From v_{res} the resonance energy E_{res} can be found. This has been done for selected times of the events listed above. The results are shown in Figure 10. These results confirm our general conclusion that $\omega/k_\parallel$ corresponds to resonance energies in the kilovolt range, with wavelengths of a kilometer or greater. A few of the measured $|B|^2/|E|^2$ ratios get high enough to challenge the basic assumption that auroral hiss is propagating near the resonance cone, although most do not. Interestingly, the lowest resonance energy computed, around 0.3 keV, corresponding to about 300-m wavelength, was measured in a density cavity. The resonance energy at this point agrees well with beam energies that are usually observed in the auroral region, several hundred electron volts. The idea that auroral hiss is generated by beams of a few hundred electron volts and then converted to higher resonance energies by refraction over density boundaries will be discussed in the last section.

Thus the intensity difference between poleward and equatorward auroral hiss, to some extent, can be attributed to the existence of a high-energy tail in the electron distribution equatorward of the source region. The fact that auroral hiss is often observed propagating at low intensity through the plasmasphere indicates that some auroral hiss waves are propagating at values of $\omega/k_\parallel$ sufficiently large to avoid damping by the high energy tail of the electron distribution. Unfortunately, the HAPI data do not indicate the maximum extent of the high energy tail.

Table 4 shows values of the damping calculated for $\omega/k_\parallel = 2.3 \times 10^4$ km/s (resonance energy 1.5 keV) at three different frequencies. The result of this computation is that the damping is greater at higher frequency. Thus high-frequency radiation should be damped closer to the source than low-frequency radiation, implying a downward sloping intensity profile as one moves away from the source. This type of intensity variation with frequency can be seen in the spectrogram for the event of September 26, 1981, shown in Plate 2. The effect occurs around 65° INV where the auroral hiss appears to have a sharply descending intensity drop. The effect is somewhat obscured by an increase in auroral hiss intensity that appears to be due to another source. Other events with intensity profiles of this type have been observed, mostly on the nightside. On the other hand, the attenuation in Plate 3 at 67° INV is constant across the bandwidth of the auroral hiss. The attenuation may be due to a reflection effect, or the downward sloping intensity profile may be obscured by multiple sources. Another possibility is that the downward slope may take place on a small enough spatial scale that the 32-s sweep time of PWI cannot resolve it. Although the downward sloping intensity profile can be obscured by source geometry and other effects, the existence of such a profile should be taken as an indication that Landau damping is occurring.

6. Discussion and Conclusions

The study in the previous section indicates that Landau damping is an important effect to be considered in the propagation of auroral hiss. Studies of the variation of damping with resonance velocity indicate that on the poleward side of the auroral hiss source region in the auroral zone, values of $\omega/k_\parallel = 3.4 \times 10^4$ km/s or greater, corresponding to resonance energies of 3 keV or greater, are generally required to avoid significant damping of auroral hiss. These resonance velocities correspond to wavelengths of the order of 2 km or greater. On the equatorward side, significant damping is always predicted for resonance energies of 10 keV or less. For auroral hiss to propagate equatorward with negligible damping it must have wavelengths greater than 3 km.

These results lead to a serious question concerning the generation of upgoing auroral hiss, namely, where are the beams needed to generate hiss at these resonance energies? Upgoing beams of several kilovolt energy are rarely visible in the particle data. In one case a faint beam of about 7 keV has been detected on the poleward edge of the auroral zone during the October 5, 1981, event. Usually, however, beam energies are of the order of a few hundred volts. According to our calculations, auroral hiss from such beams should be heavily damped going either poleward or equatorward. In a study by *Lin et al.* [1984] the existence of dayside auroral hiss has been correlated with the occurrence of 100-eV electron beams. No such correlation was found at kilovolt beam energies. On the nightside, *Laaspere and Hoffman* [1976] found that the existence of auroral hiss correlated better with the occurrence of field aligned electrons at energies less than 1 keV than with electrons at higher energies. *Hultqvist et al.* [1988], have observed with the Viking spacecraft near-kilovolt upward electron and ion beams at auroral invariant latitudes in the morning sector, but these beams have no known association with auroral hiss.

Thus the results of these Landau damping computations highlight some problems with the standard model of auroral hiss generation and propagation. First, auroral hiss must be propagating at longer wavelengths than has previously been suggested. Waves of wavelength shorter than 2 km are damped immediately both poleward and equatorward of the source. Second, long wavelengths imply beams of higher energy than are generally seen. We next discuss some possible explanations of this discrepancy.

1. The spacecraft is flying either east or west of a localized field-aligned electron beam that is sufficiently energetic to generate auroral hiss of the required wavelengths.

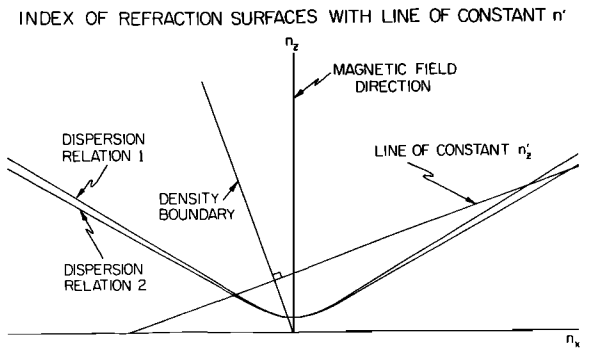

Figure 11. Possible mechanism for converting whistler mode radiation generated by a 100-eV beam into radiation with small enough wave number to escape damping. Density fluctuation is perpendicular to line of constant n'_z, 20° from the magnetic field line.

If the source of radiation is a localized beam, then the observer should not expect to see it all or even most of the time. The emission lobe profile of whistler mode noise created by a localized beam extended along a magnetic field line should take the shape of a solid cone in space. The spacecraft would then trace a line through this cone, and only by coincidence would one observe the source beam.

The association of downgoing auroral hiss with auroral arcs makes it seem likely that the source has a sheetlike rather than the localized linelike geometry that is required by the foregoing explanation. The likelihood that the geometry of the upgoing auroral hiss source region is sheetlike is reinforced by the observation that over the polar cap, the auroral hiss intensity does not appear to vary as the inverse of the source to spacecraft distance. However, other explanations may account for this fact and the association of auroral hiss with visible auroral arcs has been made only for downgoing auroral hiss. It is not clear that upgoing auroral hiss is associated with the same source as downgoing auroral hiss.

2. The beam is unnecessary and auroral hiss can be generated by mode conversion from some other mode of radiation. In fact, auroral hiss is almost always seen together with broadband electrostatic noise in the same region. Unfortunately, the mode of propagation of the broadband electrostatic noise is not known, so it is difficult at present to assess this hypothesis. Broadband noise may not be a wave at all but instead may be caused by the spacecraft traversing spatial variations in quasi-static auroral region electric fields. The broadband electrostatic noise may then indicate the cause of electron beams and, indirectly, auroral hiss. In this regard, it should be noted that sometimes radiation that looks like the higher frequency band of broadband electrostatic noise has a magnetic component. These emissions may be whistler mode emissions propagating very close to the magnetic field direction and at large resonance velocities, as suggested by *Calvert and Hashimoto* [1990]. If such emissions are generated by a Landau resonance, the existence of high-energy beams is required.

3. Auroral hiss is transformed in wavelength by partial transmission at a boundary in the index of refraction caused by an abrupt change in the plasma density. Because nightside density cavities, investigated by *Persoon et al.* [1986], are a well-known phenomenon, and data from the Viking spacecraft [*Kintner et al.*, 1987; *Holmgren and Kintner*, 1990; *Hilgers*, 1992] confirm the idea that structure in a density cavity can vary on scales of less than 1 km, this idea is very plausible. For this reason, we will explore this idea somewhat more completely.

The idea of an abrupt wavelength conversion of whistler mode waves due to transmission across a density irregularity parallel or oblique to the magnetic field has already been discussed by *Bell and Ngo* [1990]. Their discussion is for whistler mode noise not near the resonance cone, so that their analysis involves four possible rays. In adapting this idea to the present problem there will be only two possible rays for each medium, since we are dealing only with propagation near the resonance cone.

The wavelength conversion mechanism is based on the principle of the Poeverlein construction; that is, the component of the index of refraction parallel to the interface between two regions of differing index of refraction remains constant as a ray crosses the interface. This is just Snell's law. However, now instead of dealing with a gradual change while moving along the magnetic field direction, we are concerned with an abrupt change, on the scale of a wavelength or less, in the direction perpendicular to the magnetic field. The density irregularity can be considered to run either parallel or oblique to the magnetic field line. Under these conditions the component of the index of refraction parallel to that interface stays constant as the ray passes through the interface.

Figure 11 illustrates how this mechanism brings about a change in wavelength. The density interface is assumed to be oblique to the magnetic field by an angle of 20°. The difference between the two dispersion relations is for a 5% difference in density. This is a reasonable value to use for the density difference since observed density differences can vary from around 1% [*Kintner et al.*, 1987] to factors of 10 [*Roux et al.*, 1993]. The n'_z component is the component of the index of refraction parallel to the interface. If the interface were parallel to the magnetic field, the line of constant n'_z would also be a line of constant n_z and the only result would be a change of ray direction. The obliquity of the line of constant n'_z causes the wave to be converted from large to small index of refraction. Equation (20) implies that if k_z is smaller, the resonance velocity is larger. Figure 11 shows that an obliquity of 20° is enough to change n_z by a factor of about 3. Using (20) and converting the resonance velocity to energy gives a change in resonance energy of a factor of about 10. This means that auroral hiss generated by a 100-eV beam, a commonly observed beam energy, would be converted to auroral hiss waves with $\omega/k_z = 1.9 \times 10^4$ km/s, corresponding to a resonance energy of 1 keV.

Because the group velocity is perpendicular to the index of refraction surface, the newly created long wavelength wave is reflected back into the first medium, while the short wavelength wave is transmitted into the second medium where it is quickly damped. Thus, unfortunately, after one reflection the long wavelength wave is propagating in the wrong direction. However, a multiple-reflection mechanism can easily be invoked to get the long wavelength wave going in the right direction. Such a mechanism is sketched in Figure 12. This figure shows index of refraction diagrams for two reflections of a whistler mode wave along with the path of the ray as it reflects off of the walls of a flared density

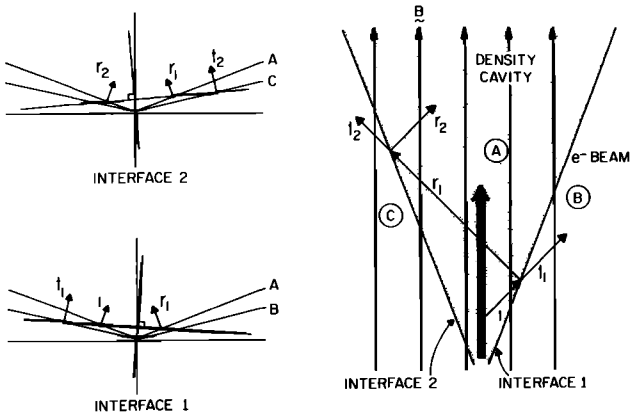

Figure 12. Multiple-reflection mechanism resulting in long wavelength waves propagating out of a density cavity that is flared in the upward direction. Labels indicate the following: i, the initial ray; r, a reflected ray; t, a transmitted ray; subscripts 1 and 2, interfaces; labels A and B, media. Ray t_2 will be the first long wavelength ray to be transmitted out of the cavity. Ray t_2 and all subsequent transmitted rays will have wavelength increased over that of the initial ray.

cavity. This diagram shows that the second and all subsequent transmitted rays have decreased n_z and therefore increased resonance velocity. One advantage of this process is that long wavelength waves would be emitted from both sides of the cavity, giving long wavelength waves propagating outwards in both directions, as observed. The flaring of the cavity shown in Figure 12 is greatly exaggerated. However, with enough reflections the waves could get to any required wavelength.

We have shown that there is a large difference between the damping of auroral hiss poleward and equatorward of the auroral zone source region. The difference is more than enough to account for observed poleward-equatorward asymmetries that are often observed in auroral hiss spectrums. In fact, it is difficult to account for cases where the equatorward auroral hiss propagates undamped for significant distances. The observed unattenuated propagation implies that auroral hiss has resonance velocities $\omega/k_\parallel > 7 \times 10^4$ km/s, corresponding to resonance energies greater than 13 keV and wavelengths greater than 3 km.

The importance of Landau damping has been explored in this paper. The results of this work raise important questions about the propagation of auroral hiss that are difficult to answer, although a number of explanations have been put forward. In particular, a partial transmission mechanism using density irregularities oblique to the magnetic field has been discussed as a possible mechanism for increasing the resonance velocity $\omega/k_\parallel$ of the waves as they escape from the auroral zone, thereby allowing relatively unattenuated propagation over large distances.

Acknowledgments. This research was supported in part by NASA grant NAG5-310 through Goddard Space Flight Center, by the University of Iowa Graduate College, SwRI DE contracts NAS5-33030 and NAS5-33031, and by the Iowa Space Grant Consortium through the National Space Grant Fellowship Program. We would like to thank Scott Boardsen for his help in evaluating some of the methods used in this work.

The Editor thanks H. E. J. Koskinen for his assistance in evaluating this paper.

References

Apostol, T. M., *Calculus*, vol. II, 2nd ed., Xerox College, Waltham, Mass., 1969.

Bell, T. F., and H. D. Ngo, Electrostatic lower hybrid waves excited by electromagnetic whistler mode waves scattering from planar magnetic-field aligned plasma density irregularities, *J. Geophys. Res.*, *95*, 149, 1990.

Budden, K. G., *The Propagation of Radio Waves*, Cambridge University Press, New York, 1985.

Burch, J. L., J. D. Winningham, V. A. Blevins, N. Eaker, W. C. Gibson, and R. A. Hoffman, High-altitude plasma instrument for Dynamics Explorer-A, in *Dynamics Explorer*, edited by R. A. Hoffman, p. 455, D. Reidel, Norwell, Mass., 1981.

Burton, E. T., and E. M. Boardman, Audio-frequency atmospherics, *Proc. Inst. Radio Eng.*, *21*, 1476, 1933.

Calvert, W., and K. Hashimoto, The magnetoionic modes and propagation properties of auroral radio emissions, *J. Geophys. Res.*, *95*, 3943, 1990.

Ellis, G. R., Low-frequency radio emission from aurorae, *J. Atmos. Terr. Phys.*, *10*, 302, 1957.

Ellis, G. R., Low frequency electromagnetic radiation associated with magnetic disturbances, *Planet. Space Sci.*, *1*, 253, 1959.

Farrell, W. M., D. A. Gurnett, P. M. Banks, R. I. Bush, and W. J. Raitt, An analysis of whistler mode radiation from the Spacelab 2 electron beam, *J. Geophys. Res.*, *93*, 153, 1988.

Farrell, W. M., D. A. Gurnett, and C. K. Goertz, Coherent Cerenkov radiation from the Spacelab 2 electron beam, *J. Geophys. Res.*, *94*, 443, 1989.

Gurnett, D. A., A satellite study of VLF hiss, *J. Geophys. Res.*, *71*, 5599, 1966.

Gurnett, D. A., and L. A. Frank, VLF hiss and related plasma observations in the polar magnetosphere, *J. Geophys. Res.*, *77*, 172, 1972.

Gurnett, D. A., and L. A. Frank, A region of intense plasma wave turbulence on auroral field lines, *J. Geophys. Res.*, *82*, 1031, 1977.

Gurnett, D. A., and U. S. Inan, Plasma wave observations with the Dynamics Explorer 1 spacecraft, *Rev. Geophys.*, *26*(2), 285, 1988.

Gurnett, D. A., S. D. Shawhan, and R. R. Shaw, Auroral hiss, Z mode radiation, and auroral kilometric radiation in the polar magnetosphere: DE 1 observations, *J. Geophys. Res.*, *88*, 329, 1983.

Gurnett, D. A., W. S. Kurth, J. T. Steinberg, P. M. Banks, R. I. Bush, and W. J. Raitt, Whistler-mode radiation from the Spacelab 2 electron beam, *Geophys. Res. Lett.*, *13*(3), 225, 1986.

Helliwell, R. A., *Whistlers and Related Ionospheric Phenomena*, Stanford University Press, Stanford, Calif., 1965.

Hilgers, A., The auroral radiating plasma cavities, *Geophys. Res. Lett.*, *19*(3), 237, 1992.

Holmgren, G., and P. M. Kintner, Experimental evidence of widespread regions of small-scale plasma irregularities in the magnetosphere, *J. Geophys. Res.*, *95*, 6015, 1990.

Hultqvist, B., et al., Simultaneous observation of upward moving field-aligned energetic electrons and ions on auroral zone field lines, *J. Geophys. Res.*, *93*, 9765, 1988.

James, H. G., VLF saucers, *J. Geophys. Res.*, *81*, 501, 1976.

Kennel, C., Low-frequency whistler mode, *Phys. Fluids*, *9*(11), 2190, 1966.

Kintner, P. M., M. C. Kelley, G. Holmgren, H. Koskinen, G. Gustafsson, and J. LaBelle, Detection of spatial density irregularities with the Viking plasma wave interferometer, *Geophys. Res. Lett.*, *14*, 467, 1987.

Landau, L. D., On the vibrations of the electronic plasma, *J. Phys.*, *10*, 25, 1946.

Laaspere, T., and R. A. Hoffman, New results on the correlation between low energy electrons and auroral hiss, *J. Geophys. Res.*, *81*, 524, 1976.

Lin, C. S., J. L. Burch, S. D. Shawhan, and D. A. Gurnett, Correlation of auroral hiss and upward electron beams near the polar cusp, *J. Geophys. Res.*, *89*, 925, 1984.

Maggs, J. E., Coherent generation of VLF hiss, *J. Geophys. Res.*, *81*, 1707, 1976.

Morozumi, H. M., A study of the auroral australis in connection

with an association between VLFE hiss and auroral arcs and bands observed at south geographical pole 1960, M.S. thesis, Univ. of Iowa, Iowa City, 1962.

Mosier, S. R., and D. A. Gurnett, VLF measurements of the Poynting flux along the geomagnetic field with the Injun 5 satellite, *J. Geophys. Res.*, *74*, 5675, 1969.

Persoon, A. M., D. A. Gurnett, and S. D. Shawhan, Polar cap plasma densities from DE 1 plasma wave observations, *J. Geophys. Res.*, *88*, 10,123, 1983.

Roux, A., et al., Auroral kilometric radiation sources: In situ and remote observations from Viking, *J. Geophys. Res.*, *98*, 11,657, 1993.

Shawhan, S. D., D. A. Gurnett, D. L. Odem, R. A. Helliwell, and C. G. Park, The plasma wave and quasi-static electric field instrument (PWI) for Dynamics Explorer-A, in *Dynamics Explorer*, edited by R. A. Hoffman, p. 535, D. Reidel, Norwell, Mass., 1981.

Smith, R. L., VLF observations of auroral beams as sources of a class of emission, *Nature*, *224*(5217), 351, 1969.

Stix, T. H., *The Theory of Plasma Waves*, McGraw-Hill, New York, 1962.

Taylor, W. W. L., Generation and propagation of electromagnetic waves in the magnetosphere, Ph.D. thesis, Univ. of Iowa, Iowa City, 1973.

Winningham, J. D., F. Yasuhara, S.-I. Akasofu, and W. J. Heikkila, The latitudinal morphology of 10-eV to 10-keV electron fluxes during magnetically quiet and disturbed times in the 2100–0300 MLT sector, *J. Geophys. Res.*, *80*, 3148, 1975.

J. L. Burch and J. D. Winningham, Southwest Research Institute, San Antonio, TX 78228. (e-mail:SPAN.SWRI::Jim;Internet.david@dews1.space.swri.edu)

D. A. Gurnett, J. D. Menietti, and D. D. Morgan, Department of Physics and Astronomy, University of Iowa, Iowa City, IA 52242. (e-mail: Internet.gurnett @iowave.physics.iowa.edu; SPAN.iowave::menietti;Internet.ddm@space.physics.uiowa.edu)

(Received December 21, 1992; revised July 19, 1993; accepted August 16, 1993.)